AIAA JOURNAL
Vol. 47, No. 2, February 2009

Improvement of Stability and Accuracy for Weighted Essentially Nonoscillatory Scheme

Yiqing Shen,* Gecheng Zha,† and Baoyuan Wang‡
University of Miami, Coral Gables, Florida 33124

DOI: 10.2514/1.37697

This paper studies the weights stability and accuracy of the implicit fifth-order weighted essentially nonoscillatory finite difference scheme. It is observed that the weights of the Jiang-Shu weighted essentially nonoscillatory scheme oscillate even for smooth flows. An increased ε value of 10^{-2} is suggested for the weighted essentially nonoscillatory smoothness factors, which removes the weights oscillation and significantly improves the accuracy of the weights and solution convergence. With the improved ε value, the weights achieve the optimum value with minimum numerical dissipation in smooth regions and maintain the sensitivity to capture nonoscillatory shock profiles for the transonic flows. The theoretical justification of this treatment is given in the paper. The wall surface boundary condition uses a half-point mesh so that the conservative differencing can be enforced. A third-order accurate finite difference scheme is given to treat wall boundary conditions. The implicit time-marching method with unfactored Gauss–Seidel line relaxation is used with the high-order schemes to achieve a high convergence rate. Several transonic cases are calculated to demonstrate the robustness, efficiency, and accuracy of the methodology.

Nomenclature

C_k	=	optimal weight
IS_k	=	smoothness estimator
J	=	Jacobian of transformation
M	=	Mach number
Pr	=	Prandtl number
Pr_t	=	turbulent Prandtl number
p	=	pressure/power used for weighted essentially nonoscillatory scheme
q_k	=	heat flux in Cartesian coordinates/third-order polynomial interpolation
Re	=	Reynolds number
t	=	time
u, v, w	=	velocity components in x, y, and z direction
x, y, z	=	Cartesian coordinates
γ	=	ratio of specific heats
ΔU	=	difference of the conservative variables
ε	=	parameter introduced in weighted essentially nonoscillatory scheme
μ	=	molecular viscosity
μ_t	=	turbulent viscosity
ξ, η, ζ	=	generalized coordinates
ρ	=	density
ω_k	=	weight

Subscripts

i, j, k	=	indices
w	=	wall
∞	=	freestream

Superscripts

L, R	=	left and right sides of the interface
n	=	time level
$*$	=	dimensionless variable

I. Introduction

BECAUSE the application of computational fluid dynamics (CFD) is more and more popular, the demand for high-accuracy and high-efficiency CFD solutions is increased to satisfy the needs of broad engineering problems. So far, most of the engineering applications employ the second-order numerical accuracy. The high-order schemes (higher than third order) are mostly limited to the fundamental research such as high-fidelity turbulence simulation [e.g., large eddy simulations (LES) and direct numerical simulation (DNS)] and aeroacoustic calculation. The reason is that the high-order schemes are generally not mature enough for robust engineering applications. For example, when a high-order scheme is used, the convergence for a steady-state solution is usually difficult. How to make a high-order scheme converge well is not well studied.

For aerospace engineering applications with shock waves or contact surfaces, the essentially nonoscillatory (ENO) or weighted essentially nonoscillatory (WENO) schemes are attractive for their capability to capture discontinuities and achieve consistent high-order accuracy in smooth regions. By using a convex combination of all candidate stencils to replace the smoothest stencil of the ENO scheme, a WENO scheme has more advantages over its ENO counterpart. For example, it approaches certain high-order accuracy in smooth regions and has a better convergence rate due to the smoother numerical flux used. From its appearance [1,2] to present, the WENO schemes have been extensively applied to different flow problems in many areas.

Titarev and Toro [3] were the first to carry out an extension of the finite volume WENO schemes to three space dimensions with high-order accuracy. A finite volume WENO scheme has a higher computational cost than a WENO finite differencing scheme. A WENO finite difference method is more efficient in multidimensional calculation due to avoiding the Gaussian integrals. As pointed out in [3,4], when the piecewise parabolic reconstruction is used in two space dimensions, a finite volume WENO scheme

Presented as Paper 4431 at the 25th AIAA Applied Aerodynamics Conference, Miami, FL, 25–28 June 2007; received 24 March 2008; revision received 24 September 2008; accepted for publication 31 October 2008.

*Research Scientist, Miami Wind™, Department of Mechanical and Aerospace Engineering; yqshen@miami.edu. AIAA Member.

†Associate Professor, Director of Miami Wind™, Miami Wind Department of Mechanical and Aerospace Engineering; gzha@miami.edu. AIAA Senior Member.

‡Ph.D. Candidate, Miami Wind™, Department of Mechanical and Aerospace Engineering.

requires approximately 3 times more CPU time than the corresponding finite difference WENO scheme. In three space dimensions, the difference is about 9 times. Hence, for structured meshes, the finite difference WENO scheme is preferred and is adopted in this paper. In [5–7], the formally high-order accurate WENO shock-capturing method, which uses a third-order total-variation diminishing Runge–Kutta time evolution scheme, is applied to the reshocked two-dimensional single-mode Richtmyer–Meshkov instability [5], the shallow water and the open-channel flow equations [6], and to study adaptive mesh refinement techniques for multidimensional hydrodynamic simulation [7]. Sjogreen and Yee [8] used a low-dissipation sixth-order spatial and fifth-order WENO scheme with the standard fourth-order Runge–Kutta method to study the supersonic reactive flows.

In a WENO scheme, a Riemann solver is needed to capture the discontinuities. There are two ways to evaluate the Riemann solver fluxes. For WENO finite difference schemes, Shu suggested that the WENO reconstruction be directly applied to the split fluxes from the left or right [9]. In this paper, we employ a different method, which is to evaluate the conservative variables with a WENO scheme and then use the conservative variables to calculate the fluxes based on the Riemann solvers. This is similar to the MUSCL method of van Leer [10]. Nichols et al. [11] also used this method to add WENO schemes to the OVERFLOW implicit Navier–Stokes flow solver [12], which makes use of the MUSCL framework without the need for extensive code modifications.

Chen et al. [13] presented a class of implicit WENO schemes for the incompressible Navier–Stokes equations, in which the lower-upper symmetric Gauss–Seidel (LU-SGS) relaxation is used for computing steady-state solutions. Yang et al. [14] extended this method to the solutions of steady compressible Navier–Stokes equations. Cadiou and Tenaud [15] proposed an implicit WENO shock-capturing scheme for unsteady flows and applied it to one-dimensional Euler equations. The use of a WENO spatial operator not only enhances the accuracy of solutions, but also improves the convergence rate of steady-state computation compared with using the ENO counterpart. In [16,17], the factored LU-SGS is significantly less efficient than the unfactored Gauss–Seidel line relaxation method for the steady-state flow computation because the former introduces the factorization error limiting the Courant–Friedrichs–Lewy (CFL) number and convergence rate. Hence, in this paper, the implicit Gauss–Seidel line relaxation is used with the WENO scheme for the first time.

Zhang and Shu [18] found that, when a fifth-order WENO scheme combined with a Runge–Kutta time discretization is used to achieve steady-state solutions, the residuals do not drop below the truncation error level of the scheme, which is far greater than the machine zero. They noticed that the original smoothness indicator of Jiang and Shu [2] results in a small oscillation near a steady shock wave. The oscillation propagates to the smooth region and causes the residual to hang at the truncation error level, rather than to approach machine zero. They proposed a modified smoothness indicator near the shock region for the fifth-order WENO scheme, which can drive the residual to machine zero for some 1-D and 2-D problems when there is little influence from the boundary conditions. However, for the other examples, the residuals still fluctuate at the level of $10^{-2} \sim 10^{-4}$. Zhang and Shu [18] attributed the convergence difficulty to the influence of boundary conditions. At a critical point (the first derivative is zero), the first term in the Taylor series expansion of the IS_k of Zhang and Shu's modification does not satisfy the requirement of $IS_k = D[1 + \mathcal{O}(\Delta x^{r-1})]$ to achieve fifth-order accuracy. Thus, the accuracy of the scheme of Zhang and Shu [18] is only third-order at a critical point.

Henrick et al. [19] proposed a mapped WENO scheme to achieve the optimal accuracy order at the critical point of a smooth function and discussed the choice of ε value for the fifth-order WENO scheme. When ε is dominant in magnitude, the predictions of the WENO scheme approach those of the upstream central difference schemes. Furthermore, oscillation on the order of ε^2 may exist near discontinuities. Hence, if the ε is too large, it will mitigate the ENO behavior of the method to capture monotonic shock profiles. Henrick et al. suggested that ε can be slightly larger than the square root of the smallest positive number allowed for a particular machine, but they did not study the convergence behavior for computing steady-state solutions.

So far, the fifth-order WENO schemes are mostly used for unsteady flow calculation such as LES, DNS, or aeroacoustic calculation [20–23]. For unsteady calculation, if an explicit scheme such as a Runge—Kutta scheme is used, the convergence is generally not an issue. If a dual time-stepping procedure [24] is used, the convergence is required within each physical time step. However, for dual time stepping, a fixed number of iterations within each physical time step is often used and the convergence of the solution is sometimes overlooked. The best convergence test is to calculate steady-state solutions to see if they can be converged to machine zero. For transonic flows with shock wave discontinuities, little research has been done to study the convergence behavior of steady-state solutions using high-order WENO schemes.

In this paper, it is shown that the convergence difficulty of the original WENO scheme of Jiang and Shu [2] is caused by the oscillation of the weights, which also shifts the weights away from the optimum values in smooth regions and increases the diffusiveness of a WENO scheme. A WENO scheme is designed to achieve the minimum numerical dissipation in smooth regions when the weights are equal to the optimum values. The optimum weights evaluate the interface flux symmetrically from the left and right like central differencing. However, because a WENO scheme must employ a Riemann solver to calculate the interface flux, the numerical dissipation always exists, but is minimum when the optimum weights are used. In our study, it is observed that the weight oscillation and deviation from the optimum value even occur for flat-plate boundary-layer flows, which are smooth with no shock waves. This may be the reason that even the sixth-order ENO scheme can be too dissipative for DNS if care is not taken [25,26].

The purpose of this paper is twofold: 1) study the stability, convergence, and accuracy of the fifth-order WENO scheme of Jiang and Shu [2]; and 2) develop a robust, efficient, and accurate remedy for computing steady-state transonic flows with solid and fast convergence. The following novel numerical techniques are developed in this paper. First, the oscillation of the weights of WENO schemes in smooth regions can be suppressed by reasonably amplifying the parameter ε in the smoothness estimators, but still maintain the sensitivity to shock waves. This treatment can stabilize the weights at the optimum values and generate minimum dissipation, which results in solid convergence to machine zero. Second, the wall boundary treatment uses a half-point mesh so that the no-slip wall boundary condition can be accurately imposed in a conservative manner for a WENO finite difference scheme. A third-order accuracy finite difference scheme is given to treat the first mesh node on the wall. Third, the implicit time-marching method with unfactored Gauss–Seidel line relaxation is used with the high-order WENO finite difference scheme to achieve steady-state solutions with high convergence rate.

II. Numerical Method

A. Governing Equations

The normalized Navier–Stokes equations governing compressible viscous flows can be written in the Cartesian coordinate as

$$\frac{\partial U}{\partial t} + \frac{\partial E}{\partial x} + \frac{\partial F}{\partial y} + \frac{\partial G}{\partial z} = \frac{1}{Re}\left(\frac{\partial R}{\partial x} + \frac{\partial S}{\partial y} + \frac{\partial T}{\partial z}\right) \tag{1}$$

where

$$U=\begin{bmatrix}\rho\\ \rho u\\ \rho v\\ \rho w\\ \rho e\end{bmatrix},\qquad E=\begin{bmatrix}\rho u\\ \rho u^2+p\\ \rho uv\\ \rho uw\\ (\rho e+p)u\end{bmatrix},\qquad F=\begin{bmatrix}\rho v\\ \rho uv\\ \rho v^2+p\\ \rho vw\\ (\rho e+p)v\end{bmatrix}$$

$$G=\begin{bmatrix}\rho w\\ \rho uw\\ \rho vw\\ \rho w^2+p\\ (\rho e+p)w\end{bmatrix},\qquad R=\begin{bmatrix}0\\ \tau_{xx}\\ \tau_{xy}\\ \tau_{xz}\\ u_k\tau_{xk}-q_x\end{bmatrix}$$

$$S=\begin{bmatrix}0\\ \tau_{xy}\\ \tau_{yy}\\ \tau_{yz}\\ u_k\tau_{yk}-q_y\end{bmatrix},\qquad T=\begin{bmatrix}0\\ \tau_{xz}\\ \tau_{yz}\\ \tau_{zz}\\ u_k\tau_{zk}-q_z\end{bmatrix}$$

The repeated index k stands for the Einstein summation over x, y, and z. The stress τ and heat flux q are

$$\tau_{ik}=(\mu+\mu_t)\left[\left(\frac{\partial u_i}{\partial x_k}+\frac{\partial u_k}{\partial x_i}\right)-\frac{2}{3}\delta_{ik}\frac{\partial u_j}{\partial x_j}\right]$$

$$q_j=\frac{-1}{(\gamma-1)M_\infty^2}\left(\frac{\mu}{Pr}+\frac{\mu_t}{Pr_t}\right)\frac{\partial T}{\partial x_j}$$

The equation of state is

$$\rho e=\frac{p}{\gamma-1}+\frac{1}{2}\rho(u^2+v^2+w^2)$$

where μ_t is the turbulence eddy viscosity calculated by the Baldwin–Lomax model [27].

In the preceding equations, ρ is density, u, v, and w are the Cartesian velocity components in x, y, and z directions, p is static pressure, e is total energy per unit mass, μ is molecular viscosity, J is the transformation Jacobian, and γ, Re, M_∞, Pr, and Pr_t are the ratio of specific heat, Reynolds number, freestream Mach number, Prandtl number, and turbulent Prandtl number, respectively.

The dimensionless flow variables in the governing equations are defined as follows:

$$x^*=\frac{x}{L},\quad y^*=\frac{y}{L},\quad z^*=\frac{z}{L},\quad u^*=\frac{u}{U_\infty},\quad v^*=\frac{v}{U_\infty}$$

$$w^*=\frac{w}{U_\infty},\quad \rho^*=\frac{\rho}{\rho_\infty},\quad \mu^*=\frac{\mu}{\mu_\infty},\quad t^*=\frac{t}{L/U_\infty}$$

$$T^*=\frac{T}{T_\infty},\quad p^*=\frac{p}{\rho_\infty U_\infty^2},\quad e^*=\frac{e}{U_\infty^2},\quad \mu^*=\frac{\mu}{\mu_\infty}$$

where L is the reference length and the freestream conditions are denoted by the subscript ∞. For simplicity, the subscript $*$ is omitted in Eq. (1). In the generalized computational coordinates, Eq. (1) can be written as

$$\frac{\partial U'}{\partial t}+\frac{\partial E'}{\partial \xi}+\frac{\partial F'}{\partial \eta}+\frac{\partial G'}{\partial \zeta}=\frac{1}{Re}\left(\frac{\partial R'}{\partial \xi}+\frac{\partial S'}{\partial \eta}+\frac{\partial T'}{\partial \zeta}\right)\qquad(2)$$

where

$$U'=\frac{1}{J}U$$

$$E'=\frac{1}{J}(\xi_t U+\xi_x E+\xi_y F+\xi_z G)$$

$$F'=\frac{1}{J}(\eta_t U+\eta_x E+\eta_y F+\eta_z G)$$

$$G'=\frac{1}{J}(\zeta_t U+\zeta_x E+\zeta_y F+\zeta_z G)$$

$$R'=\frac{1}{J}(\xi_x R+\xi_y S+\xi_z T)$$

$$S'=\frac{1}{J}(\eta_x R+\eta_y S+\eta_z T)$$

$$T'=\frac{1}{J}(\zeta_x R+\zeta_y S+\zeta_z T)$$

For simplicity, the prime $'$ in Eq. (2) will be omitted in the rest of this paper.

Equation (2) is discretized in an implicit form as

$$\frac{1}{J\Delta t}\Delta U^{n+1}+(E^{n+1}_{i+\frac{1}{2}}-E^{n+1}_{i-\frac{1}{2}})+(F^{n+1}_{j+\frac{1}{2}}-F^{n+1}_{j-\frac{1}{2}})+(G^{n+1}_{k+\frac{1}{2}}-G^{n+1}_{k-\frac{1}{2}})$$
$$=\frac{1}{Re}[(\tilde{R}^{n+1}_{i+\frac{1}{2}}-\tilde{R}^{n+1}_{i-\frac{1}{2}})+(\tilde{S}^{n+1}_{j+\frac{1}{2}}-\tilde{S}^{n+1}_{j-\frac{1}{2}})+(\tilde{T}^{n+1}_{k+\frac{1}{2}}-\tilde{T}^{n+1}_{k-\frac{1}{2}})]\qquad(3)$$

where the inviscid numerical fluxes $E^{n+1}_{i+\frac{1}{2}}$, $F^{n+1}_{j+\frac{1}{2}}$, and $G^{n+1}_{k+\frac{1}{2}}$ are evaluated by the WENO scheme with a Riemann solver as described in Secs. II.B and II.C, and the viscous numerical fluxes $\tilde{R}^{n+1}_{i+\frac{1}{2}}$, $\tilde{S}^{n+1}_{j+\frac{1}{2}}$, and $\tilde{T}^{n+1}_{k+\frac{1}{2}}$ are evaluated by a fourth-order fully conservative central differencing described in [28].

B. Flux Difference Splitting

The Roe's flux difference scheme [29] is used as the Riemann solver with the WENO scheme in this paper. For the rest of the paper, we will take the flux in ξ direction as the example to explain the numerical methodology. Other directions can be obtained following the symmetric rule.

For the Roe scheme,

$$E_{i+\frac{1}{2}}=\tfrac{1}{2}[E(U^L)+E(U^R)-\tilde{A}(U^R-U^L)]_{i+\frac{1}{2}}\qquad(4)$$

The high-order accuracy of $E_{i+1/2}$ is obtained by achieving the high-order accuracy of the left and right conservative variables U^L and U^R using the WENO scheme described in the next section. This procedure is similar to the MUSCL scheme suggested by van Leer [10] and is adopted in both [28] and this paper.

C. Weighted Essentially Nonoscillatory Scheme

The finite difference fifth-order accuracy WENO scheme suggested by Jiang and Shu [2] is used to evaluate the conservative variables U^L and U^R. The WENO scheme for a variable u^L can be written as

$$u^L_{i+1/2}=\omega_0 q_0+\omega_1 q_1+\omega_2 q_2\qquad(5)$$

where ω_0, ω_1, and ω_2 are the weights, and the q_0, q_1, and q_2 are the third-order accuracy reconstruction of the variables in three different stencils. They are determined as follows:

$$q_0=\tfrac{1}{3}u_{i-2}-\tfrac{7}{6}u_{i-1}+\tfrac{11}{6}u_i$$

$$q_1=-\tfrac{1}{6}u_{i-1}+\tfrac{5}{6}u_i+\tfrac{1}{3}u_{i+1}$$

$$q_2=\tfrac{1}{3}u_i+\tfrac{5}{6}u_{i+1}-\tfrac{1}{6}u_{i+2}$$

and

$$\omega_k=\frac{\alpha_k}{\alpha_0+\cdots+\alpha_{r-1}}\qquad(6)$$

$$\alpha_k = \frac{C_k}{(\varepsilon + IS_k)^p}, \qquad k = 0, 1, 2 \tag{7}$$

where C_k are the optimal weights with the following values:

$$C_0 = 0.1, \qquad C_1 = 0.6, \qquad C_2 = 0.3$$

The IS_k are the smoothness estimators determined as

$$\begin{aligned} IS_0 &= \tfrac{13}{12}(u_{i-2} - 2u_{i-1} + u_i)^2 + \tfrac{1}{4}(u_{i-2} - 4u_{i-1} + 3u_i)^2 \\ IS_1 &= \tfrac{13}{12}(u_{i-1} - 2u_i + u_{i+1})^2 + \tfrac{1}{4}(u_{i-1} - 4u_i + 3u_{i+1})^2 \\ IS_2 &= \tfrac{13}{12}(u_i - 2u_{i+1} + u_{i+2})^2 + \tfrac{1}{4}(u_i - 4u_{i+1} + 3u_{i+2})^2 \end{aligned} \tag{8}$$

The ε in Eq. (7) is introduced to avoid the denominator becoming zero. Jiang and Shu's numerical tests indicate that the results are not sensitive to the choice of ε as long as it is in the range of 10^{-5}–10^{-7}. In their paper [2], ε is taken as 10^{-6}. The u^R is constructed symmetrically as u^L about $i + \frac{1}{2}$.

D. Weight Accuracy and Stability of a Weighted Essentially Nonoscillatory Scheme

In the present study, it is observed that, when there are shock waves or large gradient regions in the flowfields, the weights of Jiang and Shu's WENO scheme [2] will necessarily oscillate. The convergence of the numerical solutions is hence seriously affected. This can be seen from the numerical examples in Secs. III.C and III.D. The reason is as follows.

For WENO schemes, in either the regions of smooth flow or discontinuities, if the smoothness estimators IS_k are larger than the ε value, the weights are mainly determined by IS_k. In other words, the weights are sensitive to the IS_k. The WENO schemes are designed to expect that IS_k are uniformly small in smooth regions with about the same magnitude. The Taylor series expansion of Eq. (8) at x_i gives

$$IS_k = D[1 + \mathcal{O}(\Delta x^2)], \qquad D = u_i' \Delta x^2, \qquad k = 0, 1, 2 \tag{9}$$

Then, the weights ω_k satisfy

$$\omega_k = C_k + \mathcal{O}(\Delta x^2) \tag{10}$$

which ensures that the WENO scheme is of fifth-order accuracy.

The ε can be absorbed into the smoothness estimators if we let

$$IS_k' = \varepsilon + IS_k = D'[1 + \mathcal{O}(\Delta x^2)] \tag{11}$$

where $D' = D + \varepsilon$. Equation (11) implies that the magnitude of ε does not affect the accuracy order of a WENO scheme. However, ε should not be too large, otherwise, the sensitivity of shock stencils may be lost.

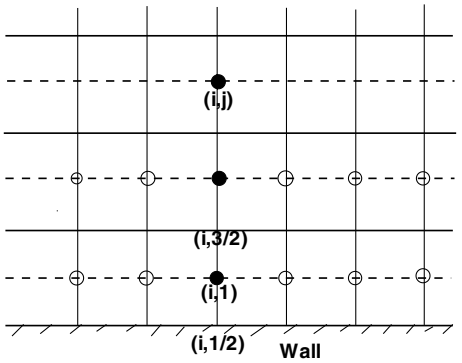

Fig. 1 Sketch of the computational grid showing the solution points located a half-cell away from the wall boundary.

Ideally, if IS_k are the same, the ω_k will be equal to the optimum weights C_k, which will give the strict fifth-order accuracy formulation defined by Eq. (5), and the optimum weights are symmetric about the interface evaluated. For example, the Q^L and Q^R in Eq. (4) will be symmetric about the interface $i + \frac{1}{2}$. For a Riemann solver such as the Roe scheme given in Eq. (4), the optimum weights C_k are the closest to the central differencing and hence generate the least numerical dissipation. When the weights ω_k are deviated from the optimum weights as defined in Eq. (10), the evaluation of the interface flux is also moved more toward one-side differencing and the numerical dissipation is hence increased, even though it is still at fifth-order accuracy. In other words, keeping the ω_k close or equal to the optimum weights C_k in smooth regions is desirable to have the minimum numerical dissipation.

Because of the nonsmoothness of flowfields, the occurrence of shock waves, and the nonuniformity of a computational mesh, the smoothness estimators IS_k can vary greatly and are not always less than the ε value, even in the smooth regions. In our numerical studies, the smoothness estimators IS_k at the probe points are 2 to 3 orders of magnitude greater than 10^{-6} in the smooth regions with no shocks. In the regions where IS_k are greater than ε, the IS_k are oscillatory and result in the oscillation of the weights. The oscillatory weights then further enhance the oscillation of the IS_k. It becomes an ill cycle and makes the solution unstable and converge poorly.

Based on Eq. (7), it can be seen that if the ε value is significantly higher than the IS_k in the smooth regions, α_k will be less sensitive to IS_k and ω_k will be closer to the optimum weights C_k. If $\varepsilon \to \infty$, the fifth-order accuracy with the optimum weights and minimum

Table 1 Accuracy of the WENO scheme with different ε

Initial	ε	N	L_∞ error	L_∞ order	L_1 error	L_1 order
$u_0(x) = \sin(2\pi x)$	$\varepsilon = 10^{-6}$	40	0.257925E-02		0.145113E-02	
		80	0.898196E-04	4.844	0.443858E-04	5.031
		160	0.278815E-05	5.010	0.138816E-05	4.999
		320	0.862413E-07	5.015	0.434416E-07	4.998
		640	0.255687E-08	5.076	0.135695E-08	5.001
	$\varepsilon = 10^{-2}$	40	0.227031E-02		0.133014E-02	
		80	0.578544E-04	5.294	0.334752E-04	5.312
		160	0.101799E-05	5.829	0.652960E-06	5.680
		320	0.154151E-07	6.045	0.111876E-07	5.867
		640	0.311103E-09	5.631	0.237542E-09	5.558
$u_0(x) = \sin^4(\pi x)$	$\varepsilon = 10^{-6}$	40	0.890319E-02		0.363465E-02	
		80	0.169913E-02	2.390	0.477658E-03	2.928
		160	0.681324E-04	4.640	0.148159E-04	5.011
		320	0.176045E-05	5.274	0.386343E-06	5.261
		640	0.287460E-07	5.936	0.908032E-08	5.411
	$\varepsilon = 10^{-2}$	40	0.699282E-02		0.335328E-02	
		80	0.219998E-03	4.990	0.102000E-03	5.039
		160	0.416665E-05	5.722	0.225675E-05	5.498
		320	0.903759E-07	5.527	0.558733E-07	5.336
		640	0.259654E-08	5.121	0.160738E-08	5.119

dissipation is ensured. The other significant benefit associated with the increased ε value is that the oscillation of IS_k and ω_k are removed. If the difference between IS_k is treated as noise, increasing ε value is similar to increasing the ratio of signal to noise.

The criterion to determine the ε value should be that ε is significantly greater than IS_k in the smooth regions so that ω_k approach C_k to have the minimum numerical dissipation. In the shock regions, ε should not be greater than IS_k so that IS_k can act to switch the scheme to one-side differencing as an ENO scheme.

In the present study, it is observed that the ε value of 10^{-2} is optimum for subsonic and transonic flows. It keeps the weights equal to the optimum value of C_k in the smooth regions, is able to identify the shock discontinuities, removes the oscillation of IS_k and ω_k, and yields stable converged solutions. The original ε value of 10^{-6} suggested by Jiang and Shu [2] generates oscillatory IS_k, large deviation of ω_k from the optimum weight C_k, significant numerical dissipation, and very poor convergence.

Obviously, the strategy of increasing the value of ε is very different from its original purpose, which was to avoid being divided by zero for the weights calculation given in Eq. (7). However, based on the aforementioned analysis, such treatment is justified with a sound theoretical foundation to improve the accuracy and stability of the fifth-order WENO scheme. The benefit will be further demonstrated by the numerical experiments given in Sec. III.

E. Time-Marching Method

The unfactored implicit Gauss–Seidel line relaxation method developed in [30–32] by the authors' research group is adopted in this paper. This is the first time that this implicit method is used with a WENO scheme.

The implicit fluxes given in Eq. (3) are treated as follows. The inviscid fluxes defined by Eq. (4) are expanded in Taylor's series about interface $i + \frac{1}{2}$,

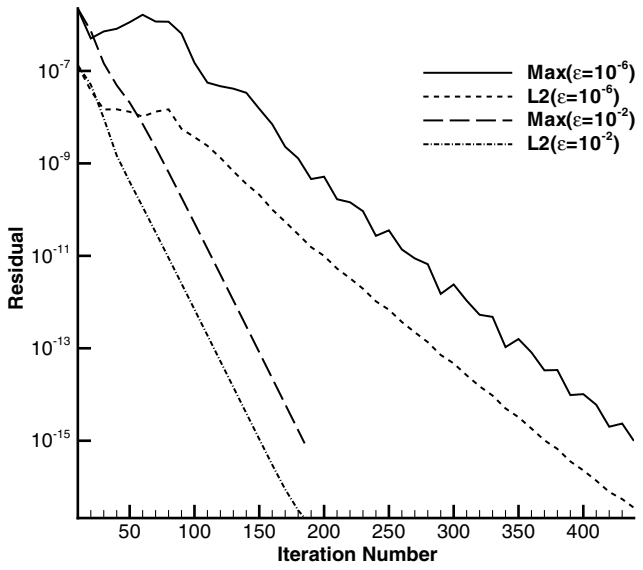

Fig. 2 Convergence histories of the supersonic boundary-layer flows with different ε values.

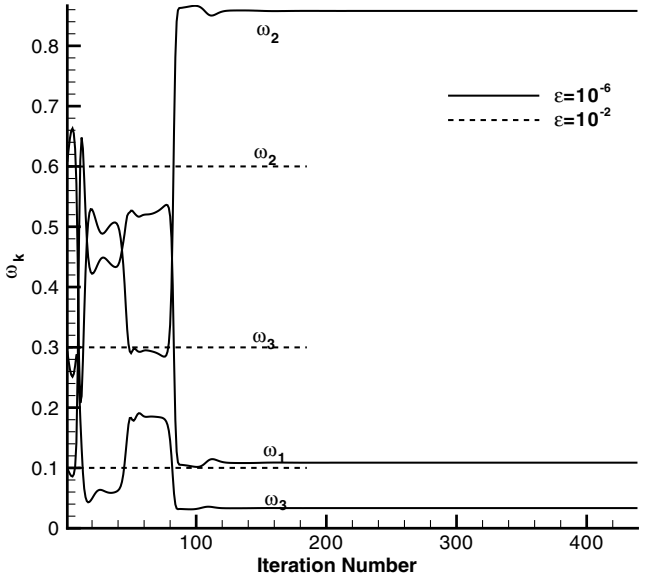

Fig. 3 Weights variation histories at the probe point (1.828, 0.467) for the supersonic laminar boundary-layer flows.

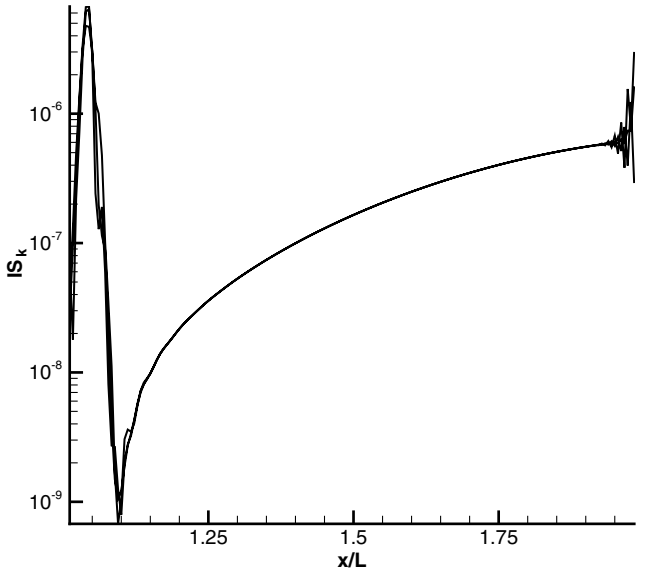

Fig. 4 Distribution of IS_k in $\rho u_{i+1/2}$ along a mesh line in the streamwise direction across the probe point (1.828, 0.467) for the supersonic laminar boundary-layer flow, $\varepsilon = 10^{-2}$.

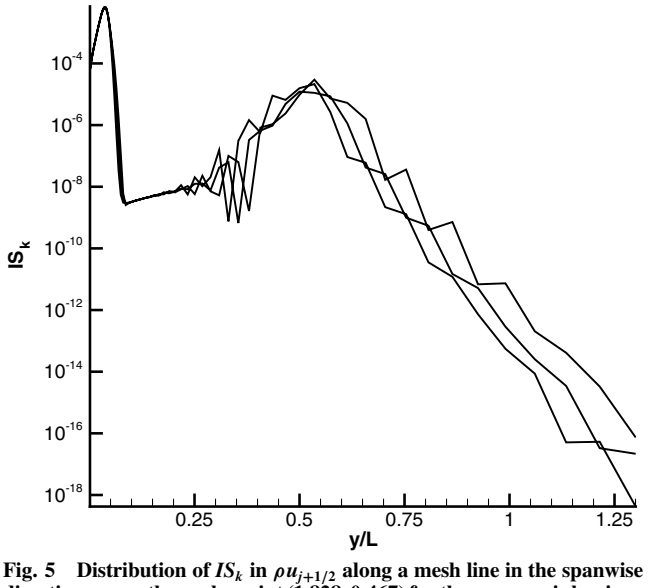

Fig. 5 Distribution of IS_k in $\rho u_{j+1/2}$ along a mesh line in the spanwise direction across the probe point (1.828, 0.467) for the supersonic laminar boundary-layer flow, $\varepsilon = 10^{-2}$.

$$E^L_{i+1/2}|^{n+1} = E^L_{i+1/2}|^n + \left(\frac{\partial E}{\partial U}\bigg|^L_{i+1/2}\right)\bigg|^n \Delta U^L_{i+1/2}|^{n+1}$$
$$= E^L_{i+1/2}|^n + A^L_{i+\frac{1}{2}}|^n \Delta U^L_{i+1/2}|^{n+1}$$
$$E^R_{i+1/2}|^{n+1} = E^R_{i+1/2}|^n + \left(\frac{\partial E}{\partial U}\bigg|^R_{i+1/2}\right)\bigg|^n \Delta U^R_{i+1/2}|^{n+1}$$
$$= E^R_{i+1/2}|^n + A^R_{i+\frac{1}{2}}|^n \Delta U^R_{i+1/2}|^{n+1}$$

and

$$\tilde{A}(U^R - U^L)|^{n+1}_{i+1/2}$$
$$= \tilde{A}(U^R - U^L)|^n_{i+1/2} + \tilde{A}_{i+1/2}|^n(\Delta U^R_{i+1/2}|^{n+1} - \Delta U^L_{i+1/2}|^{n+1})$$

The first-order approximation is used for the implicit convective terms to enhance diagonal dominance. That is,

$$\Delta U^L_{i+1/2}|^{n+1} = \Delta U^{n+1}_i, \qquad \Delta U^R_{i+1/2}|^{n+1} = \Delta U^{n+1}_{i+1}$$

The fluxes F and G are treated in the same way. The implicit viscous fluxes R, S, and T are discretized using second-order central differencing. Then, the final implicit form is as follows:

$$\bar{B}\Delta U^{n+1}_{i,j,k} + A^+\Delta U^{n+1}_{i+1,j,k} + A^-\Delta U^{n+1}_{i-1,j,k} + B^+\Delta U^{n+1}_{i,j+1,k}$$
$$+ B^-\Delta U^{n+1}_{i,j-1,k} + C^+\Delta U^{n+1}_{i,j,k+1} + C^-\Delta U^{n+1}_{i,j,k-1} = \mathrm{RHS}^n \quad (12)$$

where RHS denotes right-hand side.

The Gauss–Seidel line iteration in a certain sweep direction, for example, in ξ direction, assuming the sweeping from a small index value to a large one, can be written as

$$B^-\Delta U^{n+1}_{i,j-1,k} + \bar{B}\Delta U^{n+1}_{i,j,k} + B^+\Delta U^{n+1}_{i,j+1,k} = \mathrm{RHS}' \quad (13)$$

where

$$\mathrm{RHS}' = \mathrm{RHS}^n - A^+\Delta U^n_{i+1,j,k} - A^-\Delta U^{n+1}_{i-1,j,k}$$
$$- C^+\Delta U^n_{i,j,k+1} - C^-\Delta U^{n+1}_{i,j,k-1} \quad (14)$$

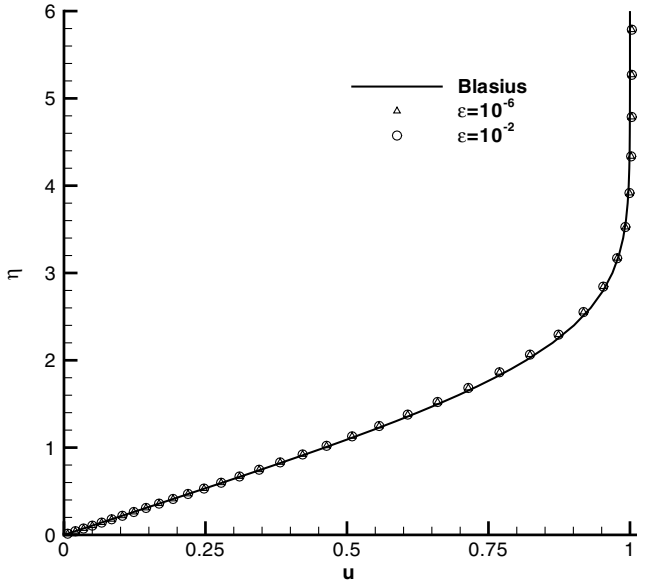

Fig. 6 Comparison of the velocity profiles of the supersonic laminar boundary-layer flows.

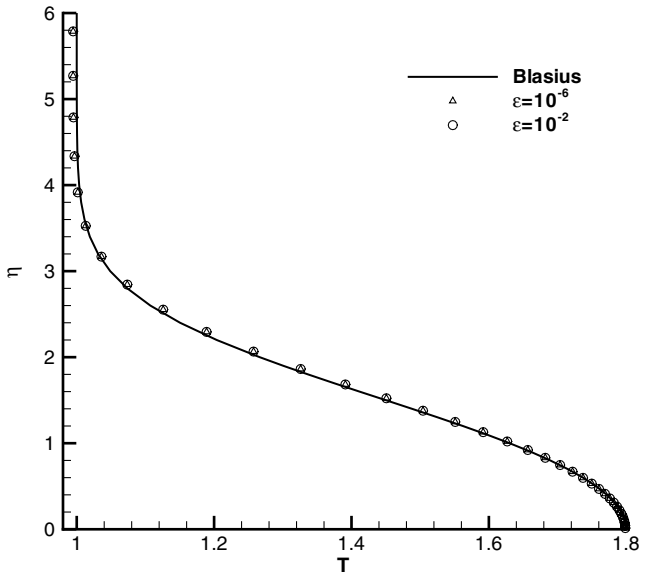

Fig. 7 Comparison of the temperature profiles of the supersonic laminar boundary-layer flows.

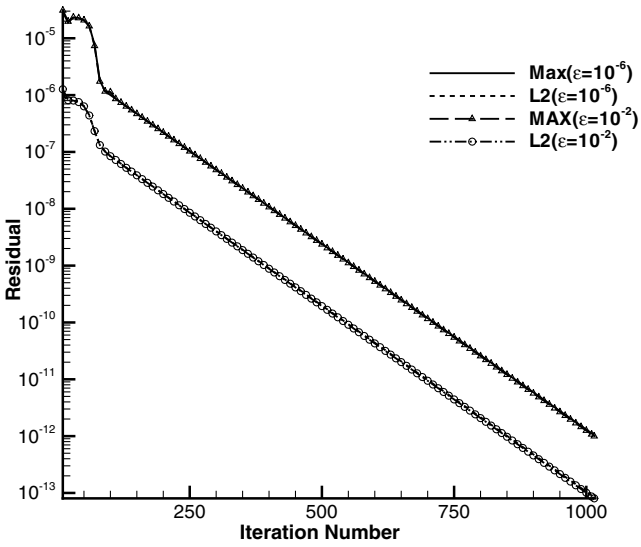

Fig. 8 Convergence histories of the subsonic flat-plate turbulent boundary-layer flows.

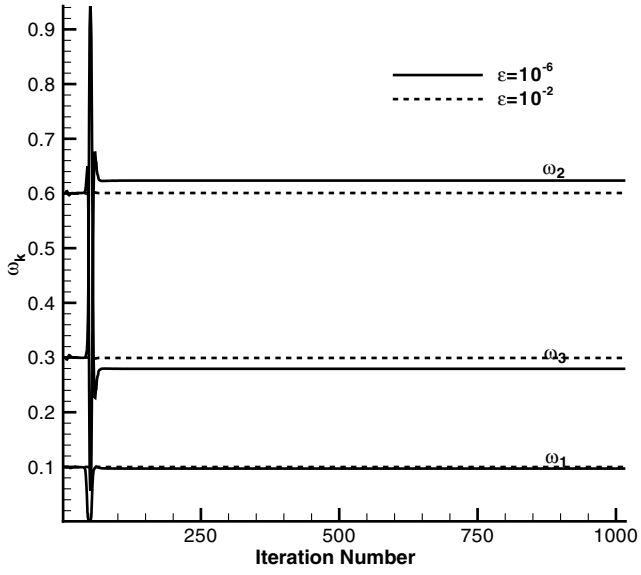

Fig. 9 Comparison of ω_k in $\rho u_{j+1/2}$ at the probe point (0.828, 0.009) vs iteration number for the subsonic flat-plate turbulent boundary-layer flows.

The accuracy of the converged solution is controlled by the RHS of Eq. (12), which is calculated by the fifth-order WENO scheme for inviscid fluxes described in Secs. II.B–II.D and the conservative fourth-order central differencing for viscous terms described in [28]. The overall accuracy of a converged solution is therefore fourth-order.

F. Wall-Boundary Treatment

Because the numerical strategy is to achieve a fully conservative finite differencing scheme, the solution points near the wall boundary are not located on the wall surface as with the conventional finite difference schemes. Instead, the solution points are located a half-mesh interval away from the wall, as illustrated in Fig. 1, similar to the finite volume treatment. For example, to calculate $\partial F/\partial\eta$ at point $(i, 1)$,

$$\frac{\partial F}{\partial \eta} = \frac{F_{i,3/2} - F_{i,1/2}}{\Delta\eta}$$

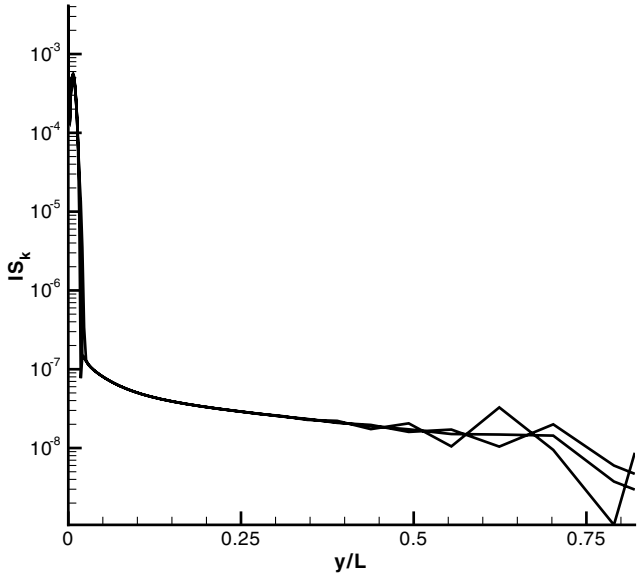

Fig. 10 Distribution of IS_k in $\rho u_{j+1/2}$ along the mesh line across the probe point for the subsonic flat-plate turbulent boundary-layer flow, $\varepsilon = 10^{-2}$.

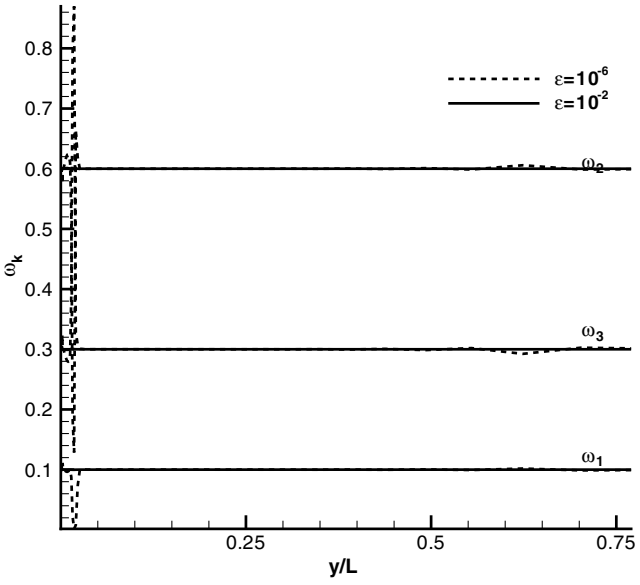

Fig. 11 Distribution of ω_k in $\rho u_{j+1/2}$ along the mesh line across the probe point for the subsonic flat-plate turbulent boundary-layer flows.

For the flux $F_{1/2}$ on the wall with a no-slip boundary condition, we have

$$F_{\frac{1}{2}} = \begin{bmatrix} \rho v|_w \\ \rho uv|_w \\ \rho v^2 + p|_w \\ \rho vw|_w \\ (\rho e + p)v|_w \end{bmatrix} = \begin{bmatrix} 0 \\ 0 \\ p|_w \\ 0 \\ 0 \end{bmatrix}$$

In this study, the third-order one-side extrapolation is used for p_w,

$$p_w = \tfrac{1}{6}(11p_1 - 7p_2 + 2p_3)$$

and the third-order reconstruction for $U^L_{i,3/2}$ and $U^R_{i,3/2}$ are used for the interface $\frac{3}{2}$,

$$U^L_{i,3/2} = \tfrac{1}{6}(2U_1 + 5U_2 - U_3), \qquad U^R_{i,3/2} = \tfrac{1}{6}(11U_2 - 7U_3 + 2U_4)$$

III. Results and Discussion

All the results presented in this section are calculated with double precision, which gives machine zero as 10^{-12}. The normalization of the Navier–Stokes equation given in Sec. II.A is to provide the order of magnitude of the flow variables, on which the discussion of the ε value of this paper is based.

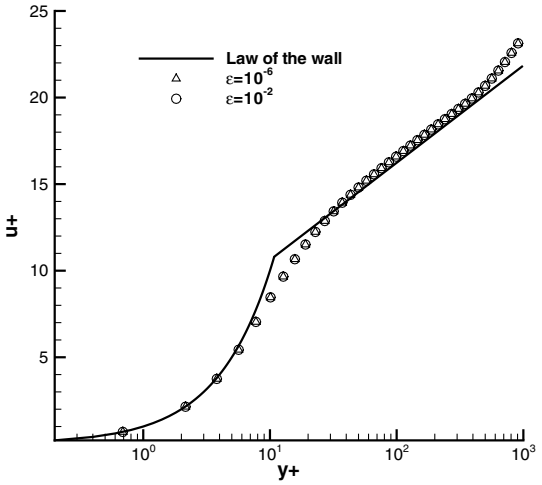

Fig. 12 Comparison of the velocity profiles of the subsonic turbulent boundary-layer flows.

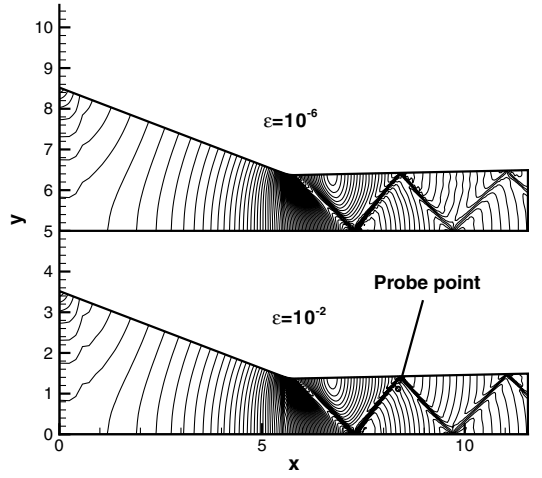

Fig. 13 Pressure contours and the probe point of the transonic converging–diverging nozzle flows.

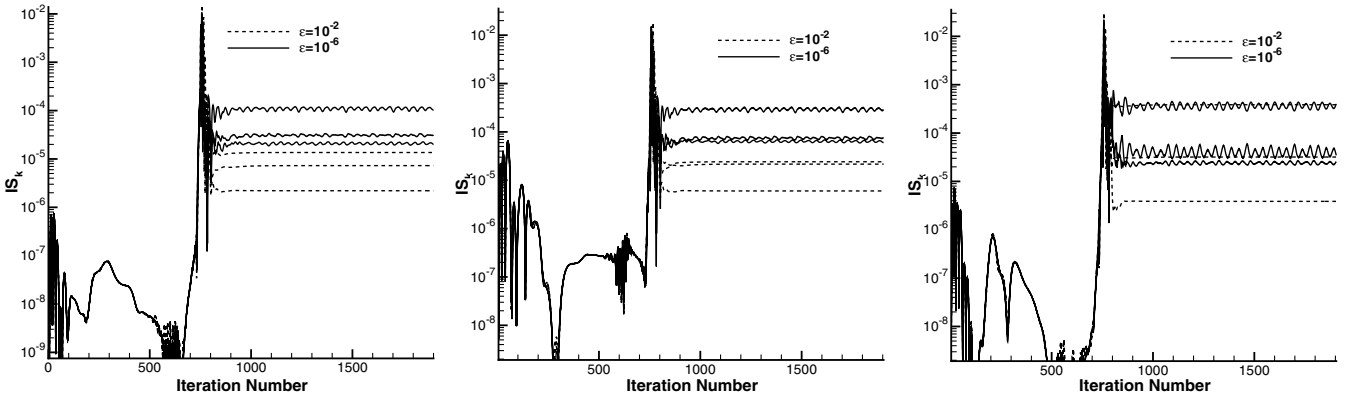

Fig. 14 Variation of IS_k vs iteration number in ξ direction at the point (8.315, 1.117) for the transonic converging–diverging nozzle flow: a) $\rho^L_{i+1/2}$, b) $(\rho u)^L_{i+1/2}$, c) $(\rho v)^L_{i+1/2}$.

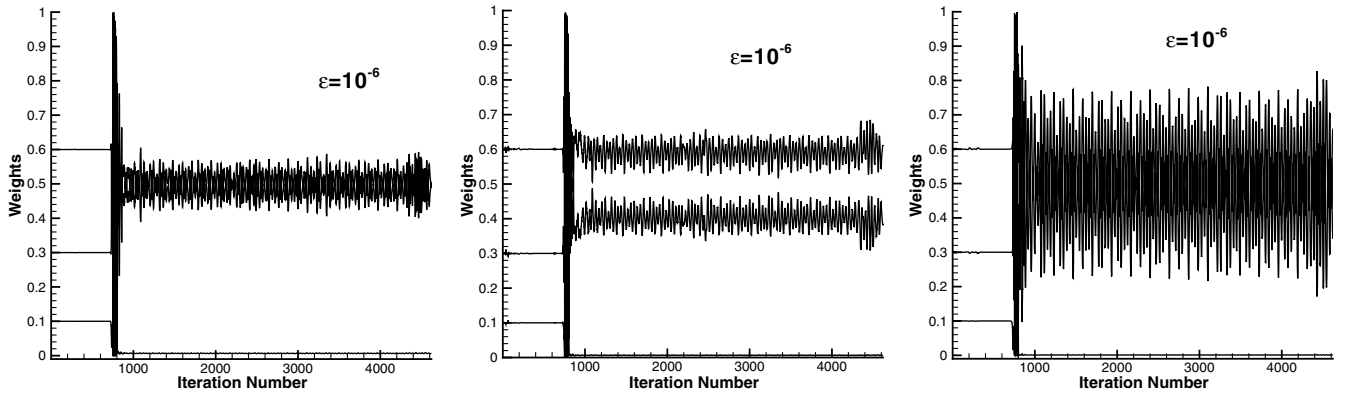

Fig. 15 Variation of weights vs iteration number in ξ direction at the point (8.315, 1.117) for the transonic converging–diverging nozzle flow, $\varepsilon = 10^{-6}$: a) $\rho^L_{i+1/2}$, b) $(\rho u)^L_{i+1/2}$, c) $(\rho v)^L_{i+1/2}$.

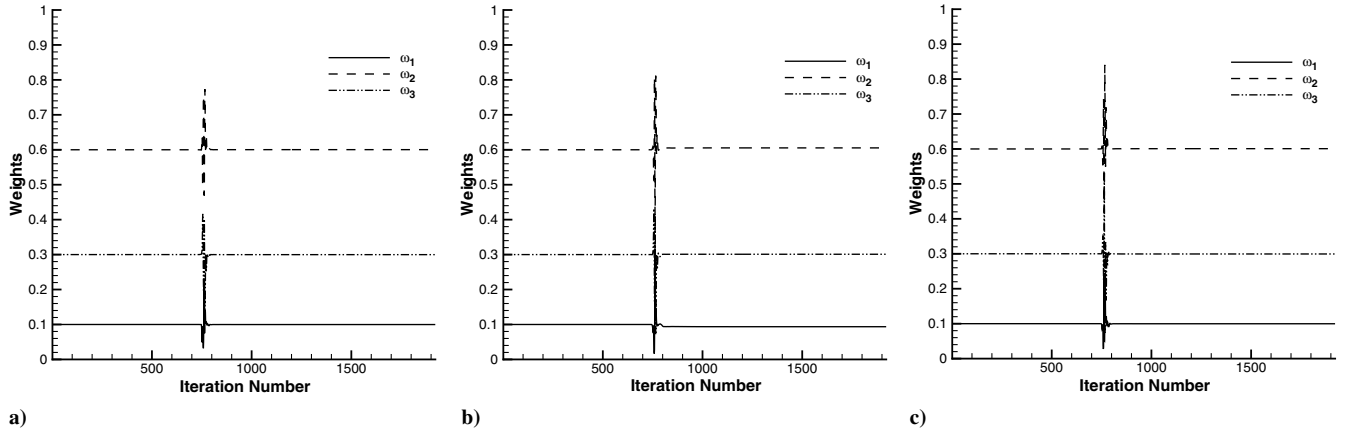

Fig. 16 Variation of weights vs iteration number in ξ direction at the point (8.315, 1.117) for the transonic converging–diverging nozzle flow, $\varepsilon = 10^{-2}$: a) $\rho^L_{i+1/2}$, b) $(\rho u)^L_{i+1/2}$, c) $(\rho v)^L_{i+1/2}$.

A. Grid Convergence and Accuracy for One-Dimensional Linear Wave Equation

To show the grid convergence of a WENO scheme with different ε values, the following wave equation

$$\frac{\partial u}{\partial t} + \frac{\partial u}{\partial x} = 0, \qquad -1 < x < 1 \qquad u(x,0) = u_0(x), \qquad \text{periodic} \tag{15}$$

with two different initial solutions $u_0(x) = \sin(2\pi x)$ and $u_0(x) = \sin^4(\pi x)$ at $t = 1$ are solved. Table 1 shows the errors and accuracy order of the WENO scheme with the two different ε values. It can be seen that the accuracy of the WENO scheme with $\varepsilon = 10^{-2}$ is fifth-order and the errors are 1 order of magnitude smaller than those of $\varepsilon = 10^{-6}$. This is consistent with the analysis and conclusion given in Sec. II.D that the increased value of ε improves the WENO scheme accuracy in smooth regions.

B. Supersonic Flat-Plate Boundary Layer

A steady-state laminar supersonic boundary-layer flow on an adiabatic flat plate is employed to test the weight accuracy, stability, and convergence of the aforementioned methodology. The incoming Mach number is 2.0. The Reynolds number based on the length of the flat plate is 4.0×10^4. The Prandtl number of 1.0 is used to compare with the analytical solution. The computation domain is taken to be $[0, 2] \times [0, 1.6]$. The mesh size is 180×80, and a CFL number of 200 is used.

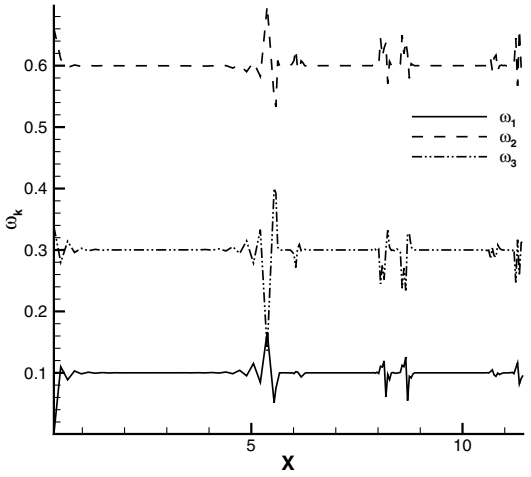

Fig. 17 Weights (in $\rho u_{i+1/2}$) distribution in the streamwise direction of the transonic converging–diverging nozzle flow, $\varepsilon = 10^{-2}$.

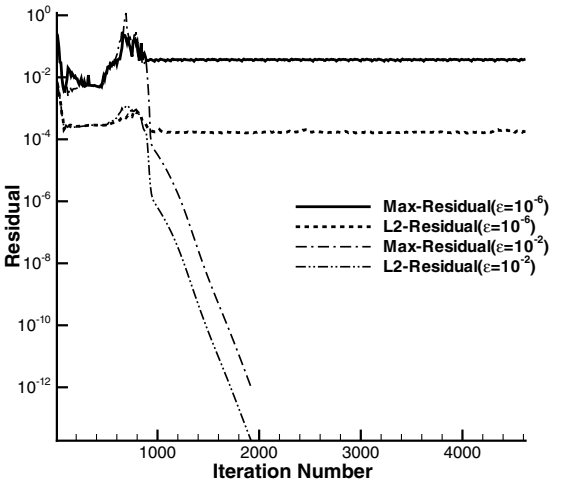

Fig. 18 Convergence histories of the transonic converging–diverging nozzle flow.

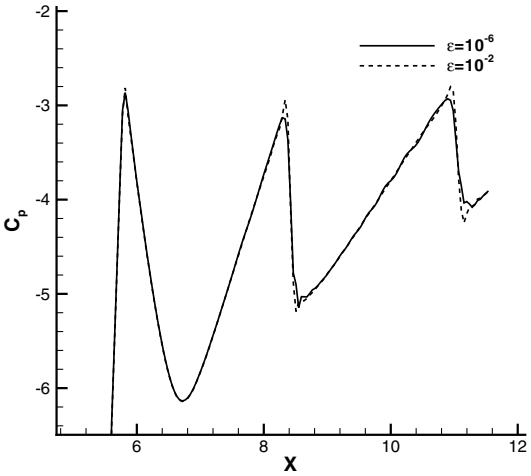

Fig. 19 Comparison of the surface pressure coefficients at the upper wall of the transonic converging–diverging nozzle flows.

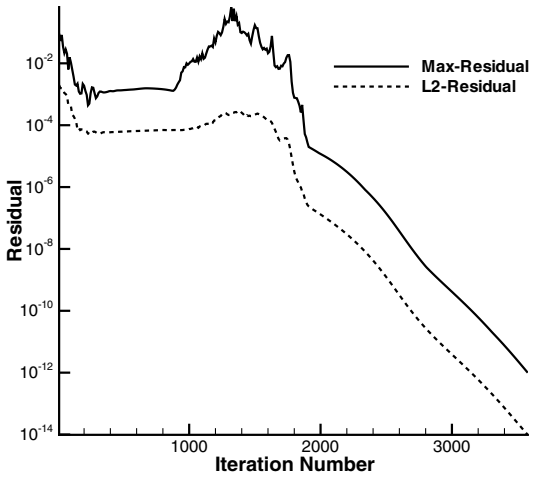

Fig. 20 Convergence history of the transonic converging–diverging nozzle flow, refined mesh size 350 × 100, $\varepsilon = 10^{-2}$.

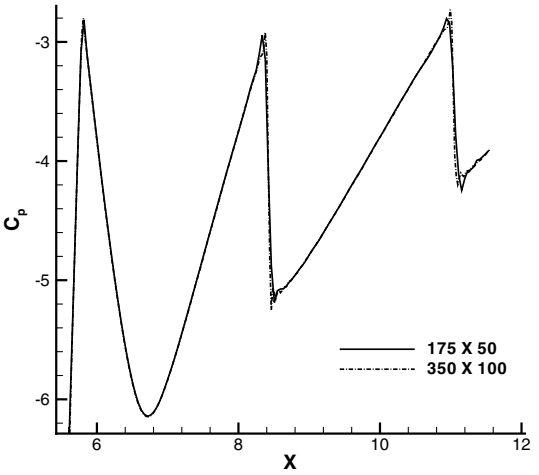

Fig. 21 Comparison of the surface pressure coefficients for the baseline mesh and refined mesh at the upper wall of the transonic converging–diverging nozzle flow, $\varepsilon = 10^{-2}$.

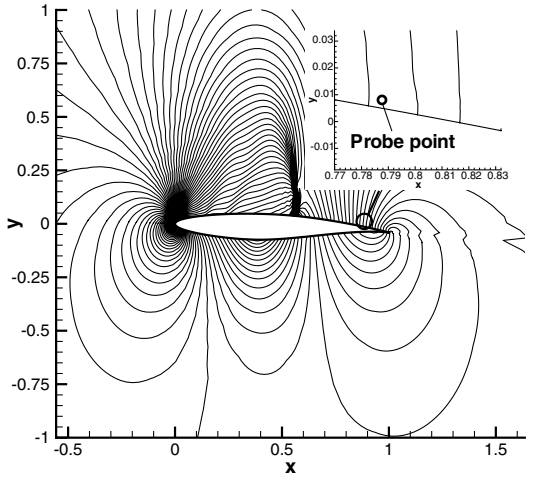

Fig. 22 Pressure contours and the probe point of the transonic flow for RAE2822 airfoil, $\varepsilon = 10^{-2}$.

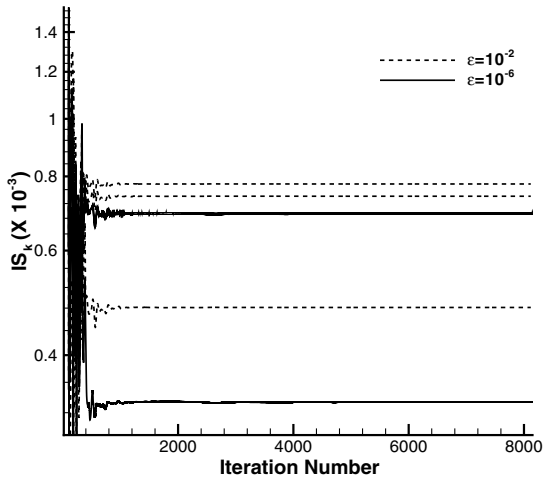

Fig. 23 Variation of IS_k in $(\rho u)^L_{j+1/2}$ vs iteration number in η direction at the point (0.789, 0.0096) for the transonic flow of RAE2822 airfoil. Fig. 23b is the zoomed plot of Fig. 23a for the IS_1.

Figure 2 shows that the convergence rate with ε of 10^{-2} is more than 2 times faster than that with the original value ε of 10^{-6}. To examine the weights behavior, a probe point is placed at the location (1.828, 0.467), which is out of the boundary layer in the uniform flow region. The reason that the ε value of 10^{-6} has slower convergence is that the weights are not stable in the beginning of the iteration process, whereas the weights with ε of 10^{-2} are basically constant, as shown in Fig. 3. Furthermore, the weights at the probe point (Fig. 3) with ε of 10^{-6} are eventually stabilized with the value of $\omega_0 = 0.109$, $\omega = 0.858$, $\omega_2 = 0.033$. They are significantly deviated from the optimal values and hence increase the numerical dissipation and degrade the accuracy even for this smooth flow. Figure 3 indicates that the weights of a WENO scheme with ε of 10^{-2} have stably secured the optimum values of 0.1, 0.6, and 0.3, which give the fifth-order accuracy with minimum numerical dissipation, as explained in Sec. II.D.

Figures 4 and 5 are the distributions of IS_k of the converged solution along the mesh lines passing through the probe point in the streamwise and spanwise direction, respectively. It can be seen in Fig. 4 that in the x direction (i.e., in $\rho u_{i+1/2}$), the IS_k are greater than 10^{-6} at the beginning and the end of the plate. In the y direction (Fig. 5 for $\rho u_{j+1/2}$), the IS_k are greater than 10^{-6} near the wall and in the middle of the computation domain. As already mentioned, the IS_k value exceeding ε will deviate the weights ω_k away from the optimum value and increase numerical dissipation.

The velocity and temperature profiles of a fifth-order WENO scheme with ε of 10^{-6} and ε of 10^{-2}, shown in Figs. 6 and 7, indicate that both numerical results agree excellently with the Blasius solution [33].

C. Subsonic Flat-Plate Turbulent Boundary Layer

The subsonic flat-plate turbulent boundary layer is used as the second 2-D test example. In this case, the Baldwin–Lomax turbulence model is used [27]. The computation domain is taken to be $[0, 1] \times [0, 1]$. The cell size is 180×80. The nondimensional distance y^+ of the first point to the wall is kept under 0.2. The inlet Mach number is 0.5, and the Reynolds number is 4×10^6 based on the plate length. The flow is subsonic at the inlet and outlet. The CFL number of 200 is used.

For this case, the convergence rates with ε of 10^{-6} and 10^{-2} are similar, as shown in Fig. 8. This can be explained by Fig. 9 showing the evolution of weights with the iteration number at the probe point $(0.828, 9.98 \times 10^{-3})$ located within the boundary layer. The weights oscillation for $\varepsilon = 10^{-6}$ only occurs on the first few iterations and then becomes stable. However, Fig. 9 shows that the weights with ε of 10^{-6} again are slightly deviated from the optimum ones. This increases the numerical dissipation. The weights with ε of 10^{-2} again have achieved the optimum values.

Figures 10 and 11 are the distribution of IS_k and ω_k of the converged solution along the mesh line in the spanwise direction through the probe point. Figure 10 shows that IS_k have the values far greater than 10^{-6} within the boundary layer with a large velocity gradient. This results in a large deviation of ω_k from the optimum ones with reduced accuracy near the wall, as shown in Fig. 11. However, for ε of 10^{-2}, the weights remain constant at the optimum values, which ensure the fifth-order accuracy with minimum numerical dissipation.

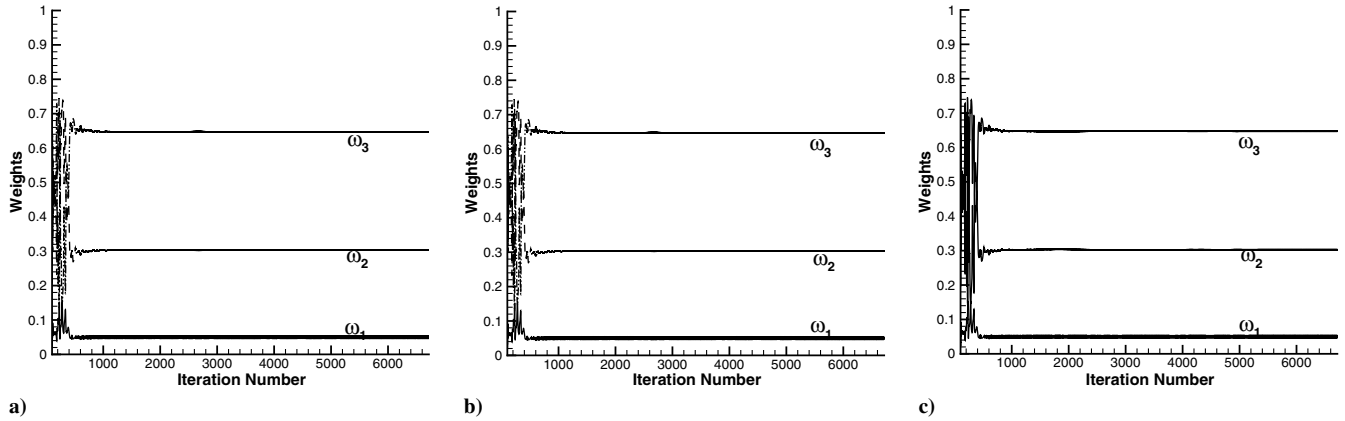

Fig. 24 Variation of weights vs iteration number in η direction at the point (0.789, 0.0096) for the transonic flow of RAE2822 airfoil, $\varepsilon = 10^{-6}$: a) $\rho^L_{j+1/2}$, b) $(\rho u)^L_{j+1/2}$, c) $(\rho v)^L_{j+1/2}$.

Figure 12 shows that the results of both the fifth-order WENO schemes with ε of 10^{-2} and 10^{-6} agree well with the law of the wall.

D. Transonic Converging–Diverging Nozzle

To examine the performance of the methodology in two-dimensional flow and the capability to capture shock waves, an inviscid transonic converging–diverging nozzle is calculated. The nozzle was designed and tested at NASA and was named nozzle A1 [34]. Because of the geometric symmetry about the center line, only the upper half of the nozzle is calculated. The mesh size is 175×50. The grid is clustered near the wall. The inlet Mach number is 0.22. The CFL number of 10 is used.

To study the effects of different ε values on the weights of Eq. (6), a probe point is located at (8.315, 1.117), which is between the two shock waves, as shown in Fig. 13.

Figure 14 gives the comparison of the variations of IS_k vs iteration number with ε of 10^{-2} and 10^{-6}. It can be seen that, when the shock is being formed at the iteration about 750, all IS_k are greater than 10^{-6}. After the shock is stabilized, the IS_k with ε of 10^{-6} are still oscillatory, whereas the IS_k with ε of 10^{-2} are very stable.

Figure 15 gives the variations of weights vs iteration number in the ξ direction with ε of 10^{-6}. It can be seen that, after the shock is formed at the iteration number about 750, the weights continue to oscillate. Figure 15 also shows that the ω_0 of the three conservative variables $\rho^L_{i+1/2}$, $(\rho u)^L_{i+1/2}$, and $(\rho v)^L_{i+1/2}$ approaches zero. Figure 15a shows that the ω_1 and ω_2 in $\rho^L_{i+1/2}$ oscillate about the value of 0.5. Figure 15b shows that, for $(\rho u)^L_{i+1/2}$, the ω_1 oscillates about the optimal weights 0.6, but ω_2 oscillates about 0.4. Figure 15c shows the weights of $(\rho v)^L_{i+1/2}$ have the similar behavior as Fig. 15b, except with the larger amplitude. With such a large oscillation of the weights with ε of 10^{-6}, the convergence of the solution is impossible.

Figure 16 gives the variations of weights vs iteration number at the same locations in ξ-direction as in Fig. 15 with ε of 10^{-2}. We can see that after the oscillation occurs at the iteration number 750 when the shock is formed, the weights ω_0, ω_1 and ω_2 return to the optimal weights 0.1, 0.6 and 0.3, respectively, and are very stable. This behavior is crucial to achieve high-order accuracy in the smooth region.

Figure 17 is the distribution of weights ω_k with ε of 10^{-2} of $\rho u_{i+1/2}$, along the grid line near nozzle centerline in the streamwise direction from nozzle inlet to exit. It shows that the shock waves and their reflections are very well captured by the weights with ε of 10^{-2}.

Figure 18 is the comparison of the convergence histories with ε of 10^{-2} and 10^{-6}. It shows that the iteration with $\varepsilon = 10^{-2}$ can converge to machine zero, whereas the residuals with $\varepsilon = 10^{-6}$ fluctuate at about the level of 10^{-2} and 10^{-4}, respectively.

In Fig. 19, the comparison of the pressure coefficients at the upper wall is illustrated. The solution of ε with 10^{-6} is more smeared for the shock profiles, even though both capture the shock locations well. From the comparison of the pressure contours shown in Fig. 13, it can be seen that the converged solution with ε of 10^{-2} is smoother than that with ε of 10^{-6}.

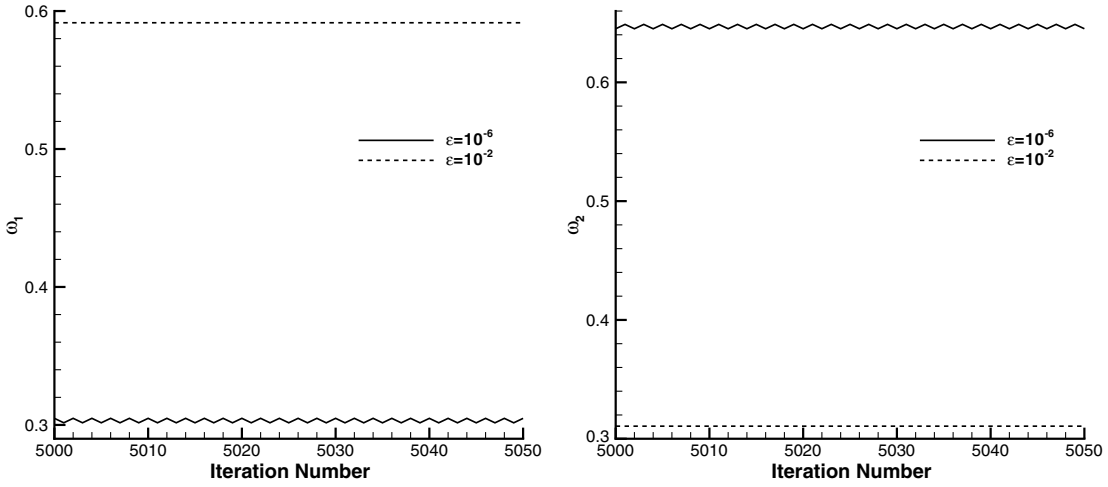

a) b)

Fig. 25 Comparison of weights in η direction at the point (0.789, 0.0096) for the transonic flow of RAE2822 airfoil: a) ω_1, b) ω_2.

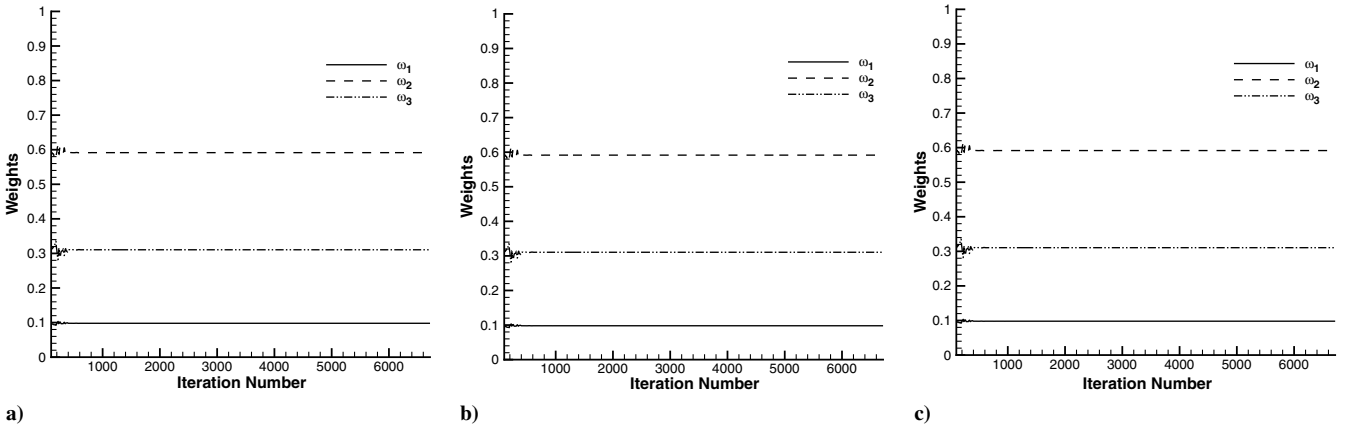

a) b) c)

Fig. 26 Variation of weights vs iteration number in η direction at the point (0.789, 0.0096) for the transonic flow of RAE2822 airfoil, $\varepsilon = 10^{-2}$: a) $\rho^L_{j+1/2}$, b) $(\rho u)^L_{j+1/2}$, c) $(\rho v)^L_{j+1/2}$.

To see the effect of the modified WENO scheme on the refined mesh with ε of 10^{-2}, Fig. 20 shows the convergence history of the refined mesh of 350×100 for the nozzle. It can be seen that the residuals are also converged to machine zero. Figure 21 is the comparison of the surface pressure coefficients of the refined mesh and the baseline mesh. The difference between the two results is very small.

E. Transonic RAE2822 Airfoil

To further examine the modified WENO scheme for transonic flows, the steady-state solution of the transonic RAE2822 airfoil is calculated using the Reynolds-averaged Navier–Stokes equations with the Baldwin–Lomax turbulence model. The mesh size is 128×55, the freestream Mach number M_∞ is 0.729, the Reynolds number based on chord is 6.5×10^6, and the angle of attack is 2.31 deg.

To study the weights variation, a probe point is located at $(x, y) = (0.789, 0.0096)$, which is downstream of the shock wave near the trailing edge, as shown in Fig. 22. Figure 23 gives the comparison of the variations of IS_k with ε of 10^{-2} and 10^{-6}. For this case, all IS_k are greater than 10^{-6}. The zoomed figure (Fig. 23b) shows that the IS_k with ε of 10^{-6} are oscillatory even though the amplitudes are small, whereas all the IS_k with ε of 10^{-2} are stable.

Figure 24 shows the variations of weights vs iteration number with ε of 10^{-6}. It can be seen that the weights oscillate largely before about 400 iterations during the shock-forming process. They become stable after that. However, the weights do not approach their optimal values ($C_0 = 0.1$, $C_1 = 0.6$, and $C_2 = 0.3$). Instead, they approach the values $\omega_0 \approx 0.05$, $\omega_1 \approx 0.3$, and $\omega_0 \approx 0.645$. Furthermore, from the zoomed plots shown in Fig. 25, it can be seen that the weights are oscillating with small amplitude when ε is 10^{-6}, whereas the weights with ε of 10^{-2} are essentially constant.

Figure 26 demonstrates the variations of weights vs iteration number in the η direction with ε of 10^{-2}. It can be seen that, after an initial oscillation with small amplitude during the shock-forming process, the weights are stabilized at their optimal values ($C_0 = 0.1$, $C_1 = 0.6$, and $C_2 = 0.3$).

Figure 27 is the distribution of IS_k in $\rho u_{i+1/2}$ with ε of 10^{-2} along a grid line through the probe point in i direction from the upstream of the airfoil to downstream. It shows that the majority of IS_k are greater than 10^{-6}, and the IS_k reach the maximum at the shock location at $x/L \simeq 0.55$. Figure 28 is the distribution of weights with ε of 10^{-2} along the same mesh line. Similar to the case 3.3, the location of the shock wave is very well captured and the weights remain at the optimum values in the smooth region.

Again, from Fig. 29, we can see that both the maximum residual and the L2 norm residual of ε equal to 10^{-6} fluctuate at the level of 10^{-2} and 10^{-5}, whereas the residuals of ε equal to 10^{-2} can be converged to machine zero.

Figure 30 is the comparison of the pressure coefficients with ε of 10^{-6} and 10^{-2} at the airfoil surface. Both results are in good agreement with the experiment, even though their convergence levels are very different, as shown in Fig. 29. The pressure contours (Fig. 22) also show that the overall flowfield with ε of 10^{-2} is smooth.

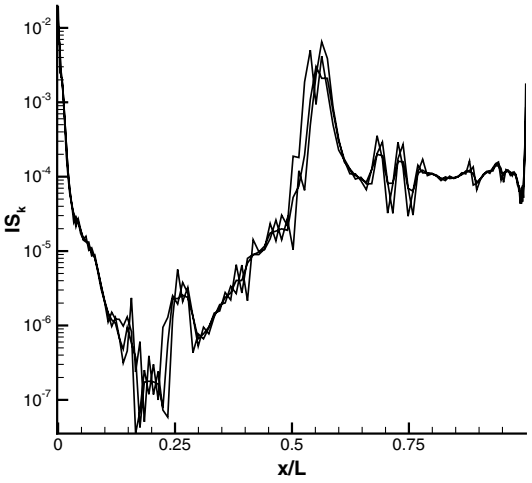

Fig. 27 IS_k distribution in $\rho u_{i+1/2}$ along i direction for the transonic flow of RAE2822 airfoil, $\varepsilon = 10^{-2}$.

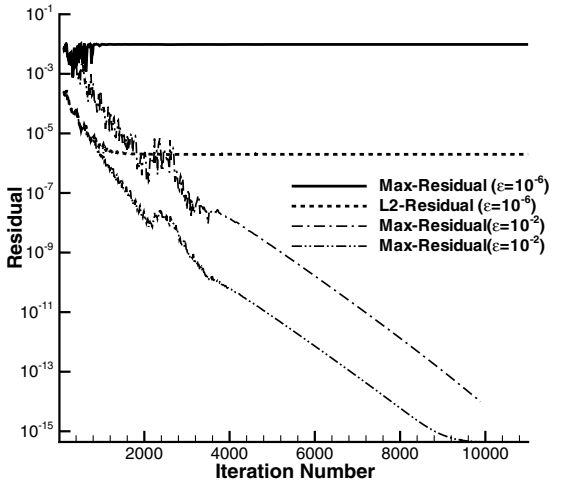

Fig. 29 Convergence histories of the transonic flow of RAE2822 airfoil.

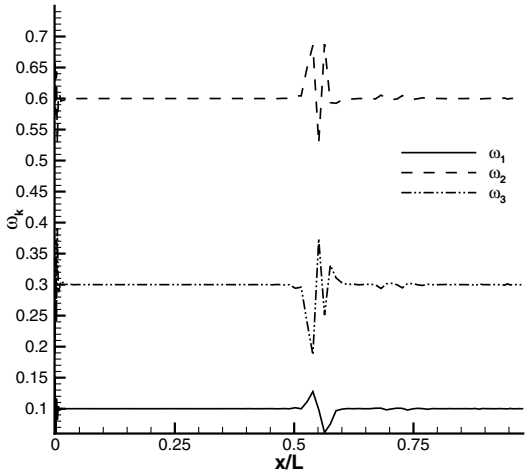

Fig. 28 Weights ω_k for $\rho u_{i+1/2}$ of the transonic flow of RAE2822 airfoil, $\varepsilon = 10^{-2}$.

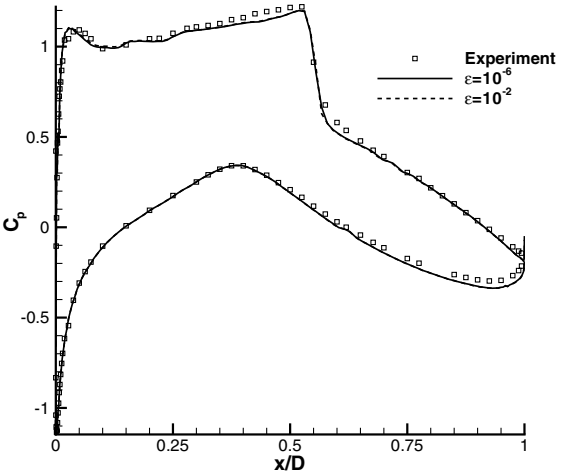

Fig. 30 Comparison of the surface pressure coefficients at the airfoil surface of the transonic flow for RAE2822 airfoil.

IV. Conclusions

This paper studies and analyzes the smoothness estimators of the fifth-order WENO scheme. It is observed for the first time that the weights of the fifth-order WENO scheme oscillate even for smooth flows due to the large variation of the smoothness estimators. The study shows that the low ε value in the smoothness estimators of the original Jiang and Shu's fifth-order WENO scheme [2] introduces weights oscillation and shift weights away from the optimum values. This problem causes a poor convergence and increases numerical dissipation. These phenomena even occur for the benign flat-plate boundary-layer flows with no shock waves. Using an enlarged ε value of 10^{-2} in the fifth-order WENO scheme removes the oscillation of the weights and significantly increases the convergence rate and level. Furthermore, ε value of 10^{-2} obtains the optimum weights in the smooth regions and yields minimum numerical dissipation and better accuracy than the original Jiang and Shu's fifth-order WENO scheme. The WENO scheme with ε of 10^{-2} maintains the sensitivity to monotonically capture transonic shock waves. The strategy of increasing the value of ε to suppress the oscillation of smoothness estimators is different from its original purpose, which was to avoid the smoothness estimators being divided by zero. The theoretical analysis given in this paper justifies this treatment to improve the accuracy and stability of the fifth-order WENO schemes.

The implicit time-marching method with unfactored Gauss–Seidel line relaxation is used with the fifth-order WENO scheme to enhance the convergence of the steady-state solutions with high convergence rate and level. The third-order wall boundary conditions with the solution points located a half-mesh point away from the wall surface enforce the conservative conditions.

The following cases are calculated to demonstrate the high-order methodology developed: 1) a flat-plate supersonic laminar boundary layer, 2) a subsonic flat-plate turbulent flow solution with Baldwin–Lomax turbulent model, 3) an inviscid 2-D converging–diverging nozzle with oblique shock waves and reflections, and 4) a turbulent transonic flow over RAE2822 airfoil. The numerical results show that the methodology suggested in this paper is efficient, robust, and accurate.

Choosing too large of an ε value will create oscillation in the shock region, which is observed in our experiment. When $\varepsilon = 10^{-1}$ is used, the solutions of the transonic converging–diverging nozzle and RAE2822 airfoil flows are oscillatory. The proposed ε value of 10^{-2} is only demonstrated to be effective for subsonic and transonic flows. It opens a door to improve the stability and accuracy of the WENO scheme. However, the effectiveness of the ε value for hypersonic flows needs to be further studied.

Acknowledgments

This work is partially supported by the U.S. Air Force Office of Scientific Research grant FA9550-06-1-0198 monitored by Fariba Fahroo and by Miami Wind™ Research Center at University of Miami.

References

[1] Liu, X. D., Osher, S., and Chan, T., "Weighted Essentially Nonoscillatory Schemes," *Journal of Computational Physics*, Vol. 115, No. 1, 1994, pp. 200–212. doi:10.1006/jcph.1994.1187

[2] Jiang, G. S., and Shu, C. W., "Efficient Implementation of Weighted ENO Schemes," *Journal of Computational Physics*, Vol. 126, No. 1, 1996, pp. 202–228. doi:10.1006/jcph.1996.0130

[3] Titarev, V. A., and Toro, E. F., "Finite-Volume WENO Schemes for Three-Dimensional Conservation Laws," *Journal of Computational Physics*, Vol. 201, No. 1, 2004, pp. 238–260. doi:10.1016/j.jcp.2004.05.015

[4] Zhou, T., Li, Y., and Shu, C. W., "Numerical Comparison of WENO Finite Volume and Runge—Kutta Discontinuous Galerkin Methods," *Journal of Scientific Computing*, Vol. 16, No. 2, 2001, pp. 145–171. doi:10.1023/A:1012282706985

[5] Latini, M., Schilling, O., and Don, W. S., "Effects of WENO Flux Reconstruction Order and Spatial Resolution on Reshocked Two-Dimensional Richtmyer-Meshkov Instability," *Journal of Computational Physics*, Vol. 221, No. 2, 2007, pp. 805–836. doi:10.1016/j.jcp.2006.06.051

[6] Crnjaric-Zic, N., Vukovic, S., and Sopta, L., "Balanced Finite Volume WENO and Central WENO Schemes for the Shallow Water and the Open-Channel Flow Equations," *Journal of Computational Physics*, Vol. 200, No. 2, 2004, pp. 512–548. doi:10.1016/j.jcp.2004.04.012

[7] Beaza, A., and Mulet, P., "Adaptive Mesh Refinement Techniques for High-Order Shock Capturing Schemes for Multi-Dimensional Hydrodynamic Simulations," *International Journal for Numerical Methods in Fluids*, Vol. 52, No. 4, 2006, pp. 455–471. doi:10.1002/fld.1191

[8] Sjogreen, B., and Yee, H. C., "Low Dissipative High-Order Numerical Simulations of Supersonic Reactive Flows," *International Journal for Numerical Methods in Fluids*, Vol. 43, Nos. 10–11, 2003, pp. 1221–1238. doi:10.1002/fld.507

[9] Shu, C. W., "Essentially Non-Oscillatory and Weighted Essentially Non-Oscillatory Schemes for Hyperbolic Conservation Laws," NASA CR-97-206253, Inst. for Computer Applications in Science and Engineering Rept. No. 97-65, Nov. 1997.

[10] Van Leer, B., "Towards the Ultimate Conservative Difference Scheme, III," *Journal of Computational Physics*, Vol. 23, No. 3, 1977, pp. 263–275. doi:10.1016/0021-9991(77)90094-8

[11] Nichols, R. H., Tramel, R. W., and Buning, P. G., "Evaluation of Two High Order WENO Schemes," AIAA Paper 2007-3920, 2007.

[12] Nichols, R. H., Tramel, R. W., and Buning, P. G., "Solver and Turbulence Model Upgrades to OVERFLOW 2 for Unsteady and High-Speed Applications," AIAA Paper 2006-2824, 2006.

[13] Chen, Y. N., Yang, S. C., and Yang, J. Y., "Implicit Weighted Essentially Non-Oscillatory Schemes for the Incompressible Navier–Stokes Equations," *International Journal for Numerical Methods in Fluids*, Vol. 31, No. 4, 1999, pp. 747–765. doi:10.1002/(SICI)1097-0363(19991030)31:4<747::AID-FLD901>3.0.CO;2-F

[14] Yang, J., Perng, Y., and Yen, R., "Implicit Weighted Essentially Non-Oscillatory Schemes for the Compressible Navier–Stokes Equations," *AIAA Journal*, Vol. 39, No. 11, 2001, pp. 2082–2090. doi:10.2514/2.1231

[15] Cadiou, A., and Tenaud, C., "Implicit WENO Shock Capturing Scheme for Unsteady Flows, Application to One-Dimensional Euler Equations," *International Journal for Numerical Methods in Fluids*, Vol. 45, No. 2, 2004, pp. 197–229. doi:10.1002/fld.685

[16] Yuan, L., "Comparison of Implicit Multigrid Schemes for Three-Dimensional Incompressible Flows," *Journal of Computational Physics*, Vol. 177, No. 1, 2002, pp. 134–155. doi:10.1006/jcph.2002.7007

[17] Shen, Y. Q., Wang, B. Y., and Zha, G. C., "Comparison Study of Implicit Gauss–Seidel Line Iteration Method for Transonic Flows," AIAA Paper 2007-4332, June 2007.

[18] Zhang, S. H., and Shu, C. W., "A New Smoothness Indicator for the WENO Schemes and Its Effect on the Convergence to Steady State Solutions," *Journal of Scientific Computing*, Vol. 31, Nos. 1–2, 2007, pp. 273–305. doi:10.1007/s10915-006-9111-y

[19] Henrick, A. K., Aslam, T. D., and Powers, J. M., "Mapped Weighted Essentially Non-Oscillatory Schemes: Achiving Optimal Order Near Critical Points," *Journal of Computational Physics*, Vol. 208, No. 1, 2005, pp. 206–227. doi:10.1016/j.jcp.2005.02.006

[20] Pantano, C., Deiterding, R., Hill, D. J., and Pullin, D. I., "A Low Numerical Dissipation Patch-Based Adaptive Mesh Refinement Method for Large-Eddy Simulation of Compressible Flows," *Journal of Computational Physics*, Vol. 221, No. 1, 2007, pp. 63–87. doi:10.1016/j.jcp.2006.06.011

[21] Taylor, E. M., and Martin, M. P., "Stencil Adaptation Properties of a WENO Scheme in Direct Numerical Simulations of Compressible Turbulence," *Journal of Scientific Computing*, Vol. 30, No. 3, 2007, pp. 533–554. doi:10.1007/s10915-006-9126-4

[22] Taylor, E. M., Wu, M., and Martin, M. P., "Optimization of Nonlinear Error for Weighted Non-Oscillatory Methods in Direct Numerical Simulations of Compressible Turbulence," *Journal of Computational Physics*, Vol. 223, No. 1, 2007, pp. 384–397. doi:10.1016/j.jcp.2006.09.010

[23] Piraux, J., and Lombard, B., "A New Interface Method for Hyperbolic Problems with Discontinuous Coefficients: One-Dimensional Acoustic Example," *Journal of Computational Physics*, Vol. 168, No. 1, 2001, pp. 227–248. doi:10.1006/jcph.2001.6696

[24] Jameson, A., "Time Dependent Calculations Using Multigrid with Application to Unsteady Flows past Airfoils and Wings," AIAA Paper 91-1596, 1991.

[25] Lee, S., Lele, S. K., and Moin, P., "Interaction of Isotropic Turbulence with Shock Waves: Effect of Shock Strength," *Journal of Fluid Mechanics*, Vol. 340, 1997, pp. 225–247. doi:10.1017/S0022112097005107

[26] Moin, P., and Mahesh, K., "Direct Numerical Simulation: A Tool in Turbulence Research," *Annual Review of Fluid Mechanics*, Vol. 30, Jan. 1998, pp. 539–578. doi:10.1146/annurev.fluid.30.1.539

[27] Baldwin, B., and Lomax, H., "Thin Layer Approximation and Algebraic Model for Separated Turbulent Flows," AIAA Paper 78-257, 1978.

[28] Shen, Y. Q., Wang, B. Y., and Zha, G. C., "Implicit WENO Scheme and High Order Viscous Formulas for Compressible Flows," AIAA Paper 2007-4431, June 2007.

[29] Roe, P., "Approximate Riemann Solvers, Parameter Vectors, and Difference Schemes," *Journal of Computational Physics*, Vol. 43, No. 2, 1981, pp. 357–372. doi:10.1016/0021-9991(81)90128-5

[30] Hu, Z., and Zha, G.-C., "Calculations of 3D Compressible Flows Using an Efficient Low Diffusion Upwind Scheme," *International Journal for Numerical Methods in Fluids*, Vol. 47, No. 3, 2005, pp. 253–269. doi:10.1002/fld.810

[31] Hu, Z. J., "Parallel Computation of Fluid-Structural Interactions Using High Resolution Upwind Schemes," Ph.D. Thesis, Dept. of Mechanical and Aerospace Engineering, Univ. of Miami, Coral Gables, FL, May 2005.

[32] Chen, X., and Zha, G.-C., "Fully Coupled Fluid-Structural Interactions Using an Efficient High Solution Upwind Scheme," *Journal of Fluids and Structures*, Vol. 20, No. 8, 2005, pp. 1105–1125. doi:10.1016/j.jfluidstructs.2005.02.011

[33] White, F. M., *Viscous Fluid Flows*, 2nd ed. McGraw–Hill, New York, 1991

[34] Mason, M. L., and Putnam, L. E., "The Effect of Throat Contouring on Two-Dimensional Converging-Diverging Nozzles at Static Conditions," NASA, TP 1704, 1980.

Z. Wang
Associate Editor